Check for updates

ChemElectroChem

Chemistry Europe
European Chemical Societies Publishing
ChemElectroChem

RESEARCH ARTICLE OPEN ACCESS

Metal–Organic Decomposition Ink-Derived Cu Foams Enable High Formate Selectivity and Methanol Conversion

Julian Neumann[1] | Vera Ubbenjans[1] | Martina Feldhoff[1] | Eric Trushin[1] | Matthias Wessling[1,2] | Robert Keller[1]

[1]Chemical Process Engineering, RWTH Aachen University, Aachen, Germany | [2]DWI - Leibniz Institute for Interactive Materials, Aachen, Germany

Correspondence: Robert Keller (robert.keller@avt.rwth-aachen.de)

Received: 19 August 2026 | **Revised:** 8 October 2026 | **Accepted:** 15 October 2026

Keywords: anode | calcination | capacitance | chemical engineering | electrode | formate | materials science | methanol | microstructure | porosity

ABSTRACT

High-surface-area electrodes are required to sustain industrially relevant current densities during selective methanol oxidation to formate. Here, particle-free Cu metal–organic decomposition (MOD) inks based on Cu(II) formate tetrahydrate and monoisopropanolamine are repurposed as solution-derived precursor coatings for porous Cu foams. Dip coating under ultrasonication and low-temperature calcination generate granular Cu structures on the foam surface and in the examined cross-sectional regions. The resulting MOD Cu foams exhibit substantially increased apparent mass-normalized double-layer capacitance and reconstruct under anodic operation into Cu(II)-rich interfaces with electrochemical behavior consistent with transient formation of Cu(III)-containing species. In zero-gap flow-cell methanol oxidation, the best-performing MOD(1:1.5) Cu foam reached a maximum formate Faradaic efficiency of 93.9% at 10% methanol conversion and a final methanol conversion of 72.2%, outperforming untreated Cu foam in both selectivity and conversion. These results establish MOD inks as a scalable route to structured Cu electrodes for selective liquid-phase electrosynthesis.

1 | Introduction

In recent years, the electrochemical methanol oxidation reaction (MOR) to formate has emerged as a promising anodic reaction for coupling with value-added cathodic processes such as electrochemical CO_2 reduction (CO_2R) [1–4]. In alkaline media, methanol (CH_3OH) is oxidized selectively to formate ($HCOO^-$), as shown in Equation (I) [5],

$$CH_3OH + 5OH^- \rightarrow HCOO^- + 4H_2O + 4e^- \quad \text{(I)}$$

MOR to formate has a thermodynamic potential of 0.103 V versus the reversible hydrogen electrode (RHE), far below the 1.23 V versus RHE required for the oxygen evolution reaction (OER) [6]. Replacing OER with MOR in paired electrolysis therefore offers a theoretical reduction in overall cell voltage of approximately 1.1 V, significantly improving energy efficiency. Beyond energetic advantages, MOR produces formate, a commodity chemical with broad applications in agriculture, textiles, leather processing, and pharmaceuticals [7]. The global demand for formic acid is projected to increase from 971.6 kt year^{-1} to 1234.8 kt year^{-1} by 2034 [7]. With a market value of approximately 829 \$ t^{-1} (North America) [8], more than twice that of methanol (350 \$ t^{-1}, North America) [9], anodic formate production can substantially enhance the economic viability of integrated electrochemical processes.

One challenge in MOR is achieving high Faradaic efficiency (FE) toward formate by suppressing anodic formation of carbonate (CO_3^{2-}). This undesired side reaction can occur either through overoxidation of formate (Equation II) [5] or via a direct oxidation pathway from methanol (Equation III) [5, 10].

$$HCOO^- + 3OH^- \rightarrow CO_3^{2-} + 2H_2O + 2e^- \quad \text{(II)}$$

$$CH_3OH + 8OH^- \rightarrow CO_3^{2-} + 6H_2O + 6e^- \quad \text{(III)}$$

Consequently, catalyst design is crucial for promoting selective formate formation while suppressing overoxidation pathways.

This is an open access article under the terms of the Creative Commons Attribution License, which permits use, distribution and reproduction in any medium, provided the original work is properly cited.

© 2026 The Author(s). *ChemElectroChem* published by Wiley-VCH GmbH.

Among the available catalyst families, Cu-based materials are particularly attractive for methanol electrooxidation to formate because they combine low cost and earth abundance [6, 11] with a reaction environment that is less biased toward complete oxidation than conventional noble metal catalysts [12]. Recent studies suggest that the comparatively moderate oxidation activity of Cu can be advantageous for steering methanol conversion toward partial oxidation products [12], while accessible Cu oxidation-state changes under anodic conditions can promote charge transfer and mediate the oxidation of adsorbed methanol through high-valent Cu species [13]. In addition, mechanistic studies on Cu surfaces indicate that formate is a comparatively stable intermediate on Cu, which further supports the use of Cu as a catalyst platform for selective formate production rather than deep oxidation to CO_2 [14]. These features make Cu-based catalysts a compelling foundation for the rational design of selective anodic methanol upgrading systems.

For industrial application, a high electrochemically active surface area (ECSA) is desirable because it reduces the local current density and cell potential, allowing higher currents to be sustained [15]. In contrast, limited ECSA can promote localized high current densities that exacerbate mass transport limitations and associated overoxidation [5]. Accordingly, maximizing ECSA while maintaining structural stability and efficient reactant transport is a central design criterion for practical MOR electrodes.

Various strategies have been developed to increase the ECSA of Cu-based electrodes, including electrodeposition, chemical or electroless surface structuring, and precursor-based coating approaches, followed by thermal conversion. These methods differ in how the active Cu phase is generated and distributed across the support, but all aim to create rough, porous, or nanostructured surfaces with a high density of accessible active sites. The following examples illustrate representative approaches that are relevant for the catalyst design discussed later in this work.

One strategy to generate high-ECSA Cu structures was introduced by Huan et al. [16], who developed a high-current electrodeposition method originally proposed for OER. By applying current densities of approximately 0.5 A cm^{-2}, simultaneous Cu deposition and vigorous gas evolution produced dendritic, highly porous morphologies with increased ECSA. Baessler et al. [5] successfully adapted this strategy to Cu foam substrates for MOR, achieving a maximum formate FE of 93% at 200 mA cm^{-2}, highlighting the benefits of dendritic Cu structures on porous supports.

A major challenge in electrodeposition on complex three-dimensional porous structures is achieving a uniform coating across the entire geometry since shielded regions are more difficult to plate effectively. In these architectures, thickness gradients arise from an inhomogeneous local current density distribution because exposed projections, corners, and outer regions experience higher current densities and therefore faster deposition, whereas recessed or shielded internal regions receive less current and develop thinner coatings [17]. In addition, electric field shielding and limited ion transport in confined regions further suppress deposition inside the structure and enhance coating nonuniformity [17, 18]. Consequently, uniform catalyst utilization together with efficient reactant transport remains a key design requirement for practical electrodeposited foam electrodes.

Alternative electroless coating strategies have been explored to overcome these constraints. Wei et al. [3] treated Cu foam in a solution of 3 M NaOH and 0.2 M ammonium persulfate at 60 °C, yielding CuO nanosheets. The resulting electrodes achieved formate FEs above 85% over an anode potential range from 1.27 to 1.59 V versus RHE, corresponding to current densities up to 200 mA cm^{-2}.

Beyond electrodeposition and electroless oxidation, metal–organic decomposition (MOD) inks provide a promising particle-free method to increase the ECSA of Cu electrodes. MOD inks were originally developed for printed and flexible electronics, where their particle-free nature is critical to avoid nozzle clogging and enable uniform processing [19–21]. Here, however, we repurpose this concept for a fundamentally different objective, namely the formation of high-surface-area Cu coatings on porous electrodes. Cu-based MOD inks typically employ Cu(II) formate as a fully soluble molecular precursor [20, 22–25]. Upon calcination, Cu(II) formate decomposes to Cu(0) with the release of CO_2 and H_2, as described in Equation (IV) [21, 22, 24].

$$Cu(HCOO)_2 \rightarrow Cu + 2\,CO_2 + H_2 \quad \text{(IV)}$$

Ligands, such as amines, can be added to the MOD ink to improve solubility of Cu(II) formate in the solvent [19] or to adjust the decomposition temperature of the MOD ink [19–21]. For Cu(II) formate, the decomposition temperature is about 200 °C [21], which can be lowered to 110 to 150 °C when bound to hexylamine or octylamine or to 80 to 110 °C when bound to pyridine [20]. In practice, the thermal conversion pathway is more complex than the simplified stoichiometry shown in Equation (IV). Amine-coordinated Cu(II) formate complexes undergo thermolysis through coupled ligand release, precursor decomposition, nucleation, and particle growth processes [20, 24, 25]. Mechanistic studies further show that Cu(II) formate decomposes through a stepwise cation reduction pathway and can involve Cu(I)-containing intermediates before full conversion to Cu(0) [21]. The coordinated amine is therefore not merely a solubilizing additive but part of the decomposition chemistry itself. Amines with lower boiling points, or weaker retention in the complex, tend to be released earlier during calcination, thereby affecting particle growth and the resulting film morphology [20, 25, 26]. The resulting Cu oxidation state and film quality are highly sensitive to the thermal and chemical environment because temperatures that are too low can lead to incomplete conversion of Cu(II) formate into Cu(0) [20, 22]. Water can further influence ink stability and Cu formation during calcination, highlighting the sensitivity of these systems to subtle changes in the ink environment [27]. To avoid oxidation during the calcination process, a protective (N_2 or Ar) or reductive (H_2) atmosphere is usually applied [21].

For printed electronics, the dominant objective has been to produce smooth, dense, and highly conductive Cu films with minimal porosity and oxide content [20, 22, 25, 26]. For electrocatalysis, however, a different morphology can be advantageous because granular structures with high roughness and interconnected porosity can increase the ECSA and improve reactant accessibility. In this context, structural features that are often regarded as

21960216, 2026, 22, Downloaded from https://chemistry-europe.onlinelibrary.wiley.com/doi/10.1002/celc.70343 by Universitatsbibliothek RWTH Aachen University, Wiley Online Library on [09/11/2026]. See the Terms and Conditions (https://onlinelibrary.wiley.com/terms-and-conditions) on Wiley Online Library for rules of use; OA articles are governed by the applicable Creative Commons License

detrimental for interconnect applications can become beneficial when Cu is used as a catalytic coating.

Relative to electrodeposition, MOD inks offer a solution-based molecular precursor route that is not inherently restricted to direct growth from electrically and ionically accessible outer surfaces. This makes them attractive as an alternative coating strategy for complex porous substrates, where a molecular precursor solution can access internal pore regions before thermal conversion. Although Cu MOD inks have been extensively developed for printed electronics [19, 20, 22, 23, 26, 28] and have recently been introduced for catalyst placement in porous gas diffusion electrodes for CO electroreduction [29], their application as solution-derived precursor coatings for self-supporting Cu foam anodes in liquid-phase methanol oxidation remains, to the best of our knowledge, unexplored.

In this work, we employ Cu MOD inks based on Cu(II) formate precursors as an alternative to electrodeposition for the fabrication of microstructured Cu anodes within complex foam architectures. The aim is to increase both the formate FE and the achievable methanol conversion during MOR by tailoring the Cu foam surface morphology through a scalable coating approach. In this way, the study explores whether MOD ink-derived Cu coatings can enhance the catalytic performance of porous Cu electrodes under industrially relevant conditions. The apparent mass-normalized double-layer capacitance, $C_{\mathrm{Dl,m}}$, is used as a relative proxy for ECSA rather than as a direct quantitative ECSA measurement.

2 | Results and Discussion

Figure 1 summarizes the four-step preparation workflow used to fabricate the MOD Cu foams, while the detailed experimental procedure is provided in the Experimental Section. The influence of the MOD ink formulation on the resulting Cu surface morphology and coating structure is discussed in the following.

MOD inks were prepared with varying molar ratios of Cu(II) formate tetrahydrate to monoisopropanolamine (MIPA) (1:1, 1:1.5, and 1:2). The resulting MOD Cu foams are referred to as MOD(1:1), MOD(1:1.5), and MOD(1:2), respectively. The influence of the MOD ink formulation on the morphology of the Cu coatings obtained after the dip coating, calcination, and cleaning procedure was investigated by scanning electron microscopy (SEM). In all cases, calcination yielded a granular, clustered Cu layer covering the majority of the foam surface. Compared to the smooth, untreated Cu foam (Figure 2a–c), the coated samples exhibited a markedly increased surface roughness. However, SEM does not allow a quantitative determination of the specific surface area or ECSA. Although the deposited Cu film partially extended over individual pores, the open three-dimensional architecture of the foam was preserved for all formulations.

For MOD(1:1) (Figure 2d–f), the coating contained some comparatively large particles of approximately 5 µm, together with smaller particles of 1 µm and in the sub-micrometer range. Increasing the MIPA content (MOD(1:1.5), Figure 2g–i) led to a pronounced reduction in the apparent particle size to below 1 µm. A further increase in MIPA content (MOD(1:2), Figure 2j–l) did not result in an additional apparent particle size refinement, indicating that particle growth is effectively limited at intermediate MIPA concentrations. Since no clear additional particle-size refinement was observed by SEM for MOD(1:2) compared with MOD(1:1.5), it was not pursued further in the electrochemical performance comparison.

Cross-sectional SEM images (Figure S1) and additional digital microscopy with extended depth of field (Figure S2) indicate penetration of the MOD ink into the porous scaffold as granular coating structures were observed not only at the outer surface but also in the examined cross-sectional regions of the foam. These qualitative measurements do not establish uniform coating thickness or loading throughout the complete three-dimensional structure.

The addition of 1 wt% polyvinylpyrrolidone (PVP) to the MOD(1:1) formulation was investigated to improve the adhesion

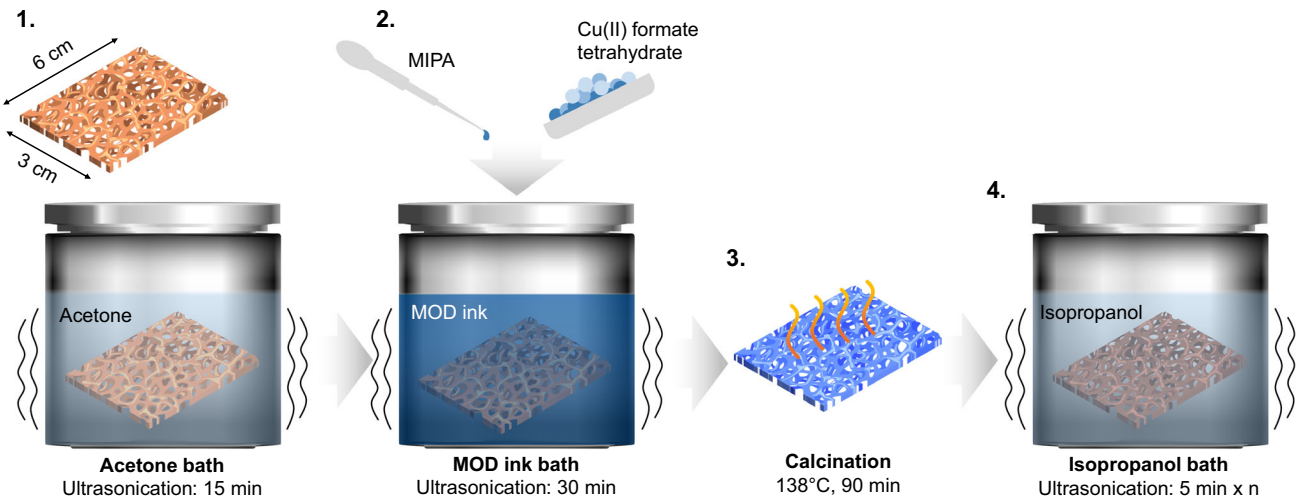


FIGURE 1 | Four-step workflow for preparing MOD Cu foams. Step 1: Cu foam was cut to the required electrode geometry, ultrasonically cleaned in acetone, rinsed with deionized (DI) water, and dried. Step 2: The Cu-based MOD ink was prepared from Cu(II) formate tetrahydrate and monoisopropanolamine (MIPA), after which the pretreated Cu foam was immersed in the freshly prepared MOD ink under ultrasonication to promote precursor infiltration. Step 3: The deposited precursor was thermally decomposed by calcination under Ar at 138 °C to form a granular Cu coating. Step 4: The coated Cu foam was cleaned by ultrasonication in isopropanol to remove residual organic species and loosely attached residues.

21960216, 2026, 22, Downloaded from https://chemistry-europe.onlinelibrary.wiley.com/doi/10.1002/celc.70343 by Universitatsbibliothek RWTH Aachen University, Wiley Online Library on [09/11/2026]. See the Terms and Conditions (https://onlinelibrary.wiley.com/terms-and-conditions) on Wiley Online Library for rules of use; OA articles are governed by the applicable Creative Commons License

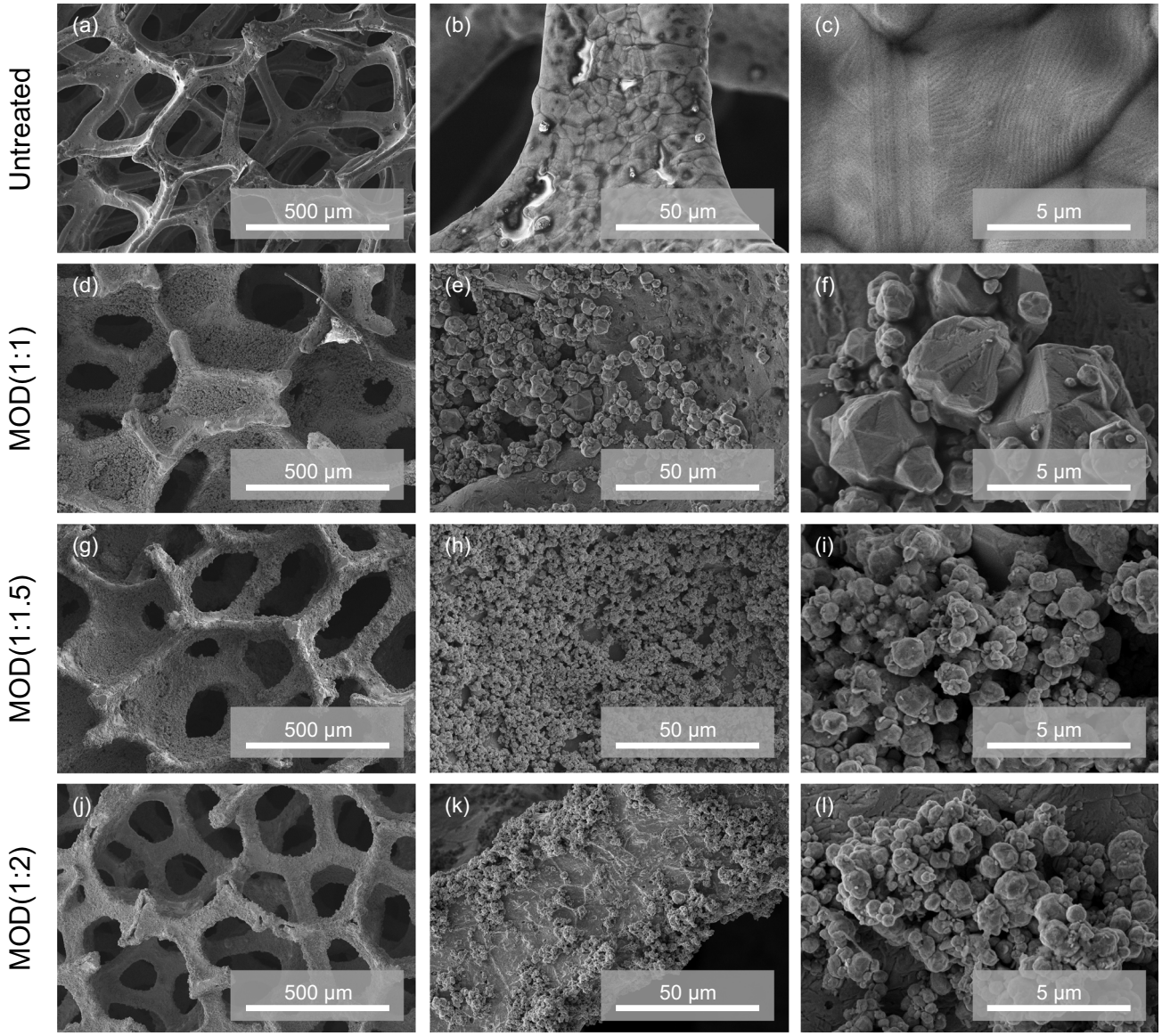


FIGURE 2 | SEM images of untreated and MOD Cu foams. The untreated Cu foam is shown in (a–c). MOD Cu foams prepared from Cu(II) formate tetrahydrate and MIPA at molar ratios of 1:1 (d–f), 1:1.5 (g–i), and 1:2 (j–l) are shown after coating, calcination, and cleaning. Images in each row are shown at increasing magnification from left to right.

of the ink to the Cu foam surface and thereby promote a more uniform and continuous coating [22]. Such improved adhesion was expected to support a more even distribution of the deposited Cu after calcination. However, SEM analysis did not reveal a noticeable improvement in coating uniformity or overall coating quality upon PVP addition (Figure S3d–f).

The addition of octylamine (OA) as a secondary ligand was also examined, motivated by literature reports describing its role in reducing the surface tension and thereby promoting the formation of smaller and more uniform Cu particles [22]. Consistent with these reports, the resulting coatings showed smaller apparent particle sizes of approximately 0.3 to 1 µm (Figure S3g–i). However, to minimize the use of hazardous chemicals in the coating approach, OA was not pursued further.

The increased roughness of the pristine MOD Cu foams already suggests a larger surface area than for the untreated Cu foam. However, because Cu surfaces are not static under anodic polarization in alkaline media, the operating interface during MOR must first be established before the capacitance and performance trends can be interpreted. Cu can undergo substantial oxidation and morphological reconstruction under these conditions, including the formation of Cu oxide or hydroxide nanostructures [30, 31].

Mechanistically, the morphological and electrochemical observations before and after MOR are consistent with the sequential oxidation of Cu under anodic conditions, progressing from Cu(0) through Cu(I)- and Cu(II)-containing surface species to highly oxidized Cu(III)-containing species. Cu(III) is widely regarded as the catalytically most reactive oxidizing state for MOR [13]. In this work, Cu(0), Cu(I), Cu(II), and Cu(III) denote formal oxidation states rather than uniquely assigned crystalline phases. In alkaline media, these oxidation states are commonly associated with representative Cu oxide, hydroxide, or oxyhydroxide motifs such as Cu_2O for Cu(I), $CuO/Cu(OH)_2$ for Cu(II),

21960216, 2026, 22, Downloaded from https://chemistry-europe.onlinelibrary.wiley.com/doi/10.1002/celc.70343 by Universitatsbibliothek RWTH Aachen University, Wiley Online Library on [09/11/2026]. See the Terms and Conditions (https://onlinelibrary.wiley.com/terms-and-conditions) on Wiley Online Library for rules of use; OA articles are governed by the applicable Creative Commons License

and CuOOH/$[Cu(OH)_4]^-$ for Cu(III) [13, 32]. Because the exact local structure, hydration state, and crystallinity of the active surface cannot be unambiguously resolved from the present ex situ characterization, the formal oxidation-state notation is used throughout the discussion.

In alkaline media, MOR on Cu is commonly described by a redox-mediated mechanism in which Cu(III)-containing species are generated electrochemically and subsequently oxidize adsorbed methanol while being reduced to Cu(II) [13, 32, 33]. The key steps can be schematically represented as follows

$$Cu^{II} \rightleftharpoons Cu^{III} + e^- \quad (V)$$

$$Cu^{III} + CH_3OH_{ads} \rightarrow Cu^{II} + HCOO^- \quad (VI)$$

This redox cycle provides a mechanistic link between the potential-dependent formation of high-valent Cu species and the onset of efficient formate production.

Postmortem SEM revealed sheet-like surface structures with lateral dimensions of 0.1 to 1 μm on all foams after MOR (Figure S4; additional high-magnification image in Figure S5). We assign these structures to Cu(II)-containing reconstruction products formed during the initial anodic polarization. This process, which is described as electrochemical hydroxylation, leads to the formation of a complex metal oxide/oxyhydroxide network that serves as the dynamically stable interface under operating conditions [34]. Similar Cu(II) sheet morphologies have been reported for chemically oxidized Cu foams [3].

Complementary X-ray diffraction (XRD) analysis of pristine and post-MOR MOD Cu foams further supports the formation of Cu(II)-containing reconstruction products during electrochemical operation (Figure S6). The pristine MOD Cu foams showed only Cu(0) reflections at 43° (Cu(111)), 50.5° (Cu(200)), 74° (Cu(220)), and 90° (Cu(311)), whereas the post-MOR samples exhibited additional reflections at 35.5° and 38.5°, assigned to CuO($\bar{1}$11) and CuO(111), respectively. These CuO reflections are consistent with the postmortem SEM observation of Cu(II)-rich sheet-like structures and confirm the formation of a crystalline CuO phase after MOR. Their higher intensity for MOD(1:1.5) compared to MOD(1:1) is consistent with more extensive formation of crystalline CuO after MOR. The interpretation of Cu(II)-containing surface reconstruction is further supported by the complementary energy-dispersive X-ray spectroscopy (EDX) and X-ray photoelectron spectroscopy (XPS) analyses described below, which provide additional information on oxygen enrichment and the Cu surface state after MOR.

To further assess the chemical changes associated with this reconstruction, EDX mapping and semiquantitative elemental analysis (Figure S7; Table S1) were performed for pristine and used MOD(1:1) and MOD(1:1.5) Cu foams. The EDX-derived oxygen fraction increased from approximately 1.6 to 4.6 at.% for the pristine MOD Cu foams to approximately 31.9–37.2 at.% after MOR in both top-view and cross-sectional measurements, providing clear evidence of pronounced oxygen enrichment after operation. The XPS survey spectra likewise show a pronounced change in the near-surface composition upon operation (Figure S8; Table S2). In addition to the increase in the relative O contribution, the Cu/O/C-normalized C contribution decreased markedly after MOR, from 75.36 to 39.40 at.% for MOD(1:1) and from 68.47 to 39.91 at.% for MOD(1:1.5). The C 1s signal may contain contributions from adventitious carbon as well as residual carbon-containing species originating from the MIPA-based MOD processing. The pronounced decrease in the relative C contribution after MOR is consistent with partial removal or oxidative decomposition of such residual carbon-containing species during electrochemical operation and electrolyte exposure. However, because the XPS atomic fractions are renormalized to Cu, O, and C, this trend does not by itself establish an absolute decrease in the amount of carbon or an unambiguous assignment of the C 1s signal to residual MIPA. The normalized atomic fractions obtained by EDX and XPS are not directly quantitatively comparable because the two techniques probe substantially different information depths and use different quantification procedures. XPS is surface sensitive, whereas EDX averages over a substantially larger interaction volume. Accordingly, the values are used comparatively within each technique rather than as absolute composition measurements.

High-resolution Cu 2p spectra (Figure S9; Table S3) show that the pristine MOD Cu foams already contain Cu(II)-containing surface species, with Cu $2p_{3/2}$ contributions at approximately 934 eV accompanied by characteristic shake-up satellite features. In combination with the absence of crystalline CuO reflections in the corresponding pristine XRD patterns, this is consistent with oxidized and hydroxylated Cu(II) surface species that are not resolved as a crystalline CuO phase by XRD, for example, because they are surface-localized and poorly crystalline. After MOR, the O 1s spectra of the used MOD electrodes (Figure S10; Table S4) exhibit a pronounced low-binding-energy contribution at 529.51 and 529.82 eV for MOD(1:1) and MOD(1:1.5), respectively, consistent with literature values reported for lattice O^{2-} in CuO [35–37]. At the same time, the Cu $2p_{3/2}$ contributions remain centered at approximately 933.6–933.9 eV and are accompanied by pronounced shake-up satellites characteristic of Cu(II) [35, 36, 38]. Although Cu 2p alone cannot unambiguously distinguish CuO from $Cu(OH)_2$, the combined EDX oxygen enrichment, Cu 2p and O 1s signatures, and the CuO reflections observed by XRD after MOR strongly support the presence of CuO within the reconstructed Cu(II)-rich surface together with additional hydroxylated oxygen species. The relative fitted O 1s component areas are model dependent and are therefore not interpreted as quantitative phase fractions. Detailed acquisition and data processing procedures for the complementary EDX and XPS measurements are provided in the Supporting Information immediately before Figure S7.

The absence of distinct Cu(III)-related reflections in the ex situ XRD patterns does not exclude the formation of Cu(III)-containing species under reaction conditions. High-valent Cu species are often amorphous or transient and may therefore not yield distinct diffraction peaks in postmortem XRD [34]. In line with this, in situ Raman studies showed that CuOOH forms only under anodic polarization and disappears after removal of the applied potential, indicating that Cu(III)-containing species are dynamically stabilized under operating bias rather than preserved ex situ [39]. This transient behavior is further supported by Deng et al., who directly identified a metastable Cu(III) oxide under anodic

21960216, 2026, 22, Downloaded from https://chemistry-europe.onlinelibrary.wiley.com/doi/10.1002/celc.70343 by Universitatsbibliothek RWTH Aachen University, Wiley Online Library on [09/11/2026]. See the Terms and Conditions (https://onlinelibrary.wiley.com/terms-and-conditions) on Wiley Online Library for rules of use; OA articles are governed by the applicable Creative Commons License

polarization using in situ Raman spectroscopy and X-ray absorption near-edge structure. The characteristic Cu(III)-related Raman feature disappeared again when the applied potential was decreased below the corresponding potential range, demonstrating the strong potential dependence of these high-valent Cu species [40]. The XRD patterns are therefore expected to predominantly reflect the relaxed Cu(II)-rich state after operation, while the electrochemical data discussed below are evaluated for consistency with transient high-valent Cu formation under anodic polarization.

To probe the evolution of Cu oxidation states and their redox transitions under controlled conditions, cyclic voltammetry (CV) was performed on a used MOD(1:1.5) Cu foam in 1 M KOH and in 1 M KOH containing 1 M methanol. In both electrolytes, the same sequence of Cu redox transitions was observed at nearly identical potentials, while the onset potential for the main anodic current shifted from 1.52 V versus RHE in 1 M KOH (OER) to 1.33 V versus RHE in 1 M KOH with 1 M methanol (MOR), reflecting the additional overpotential required by OER to drive the slower O—O bond-forming pathway (Figure 3). Accordingly, the maximum current density at 1.9 V versus RHE was substantially higher in the presence of methanol, reaching 1520 mA cm^{-2} for MOR compared to 776 mA cm^{-2} for OER.

Regarding the Cu redox behavior, all potentials from the literature were converted to the RHE scale for comparison. The first anodic peak at approximately 0.45 V versus RHE is assigned to the formation of Cu(I), followed by a second peak at approximately 0.66 V versus RHE, which is attributed to the formation of Cu(II). Both potentials are in good agreement with literature reports [13, 30, 33]. A broad anodic feature consistent with further oxidation of Cu(II) toward Cu(III) is observed between approximately 0.8 and 1.7 V versus RHE, in agreement with previously reported Cu(II)/Cu(III) redox transitions [13, 33, 41–43]. The corresponding reduction of Cu(III) to Cu(II) is not clearly resolved in either electrolyte, which is commonly reported in the literature, with values ranging from 1.475 to 1.725 V versus RHE [13, 33, 41–43].

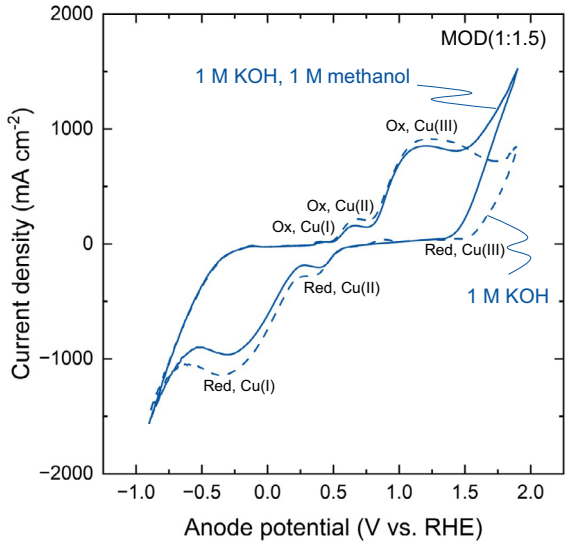


FIGURE 3 | Cyclic voltammograms of a MOD(1:1.5) Cu foam in 1 M KOH and 1 M KOH with 1 M methanol at a scan rate of 20 mV s^{-1} at room temperature.

At lower potentials, the cathodic features are assigned to the subsequent reduction of Cu(II) to Cu(I) and Cu(I) to Cu(0). The Cu(II) reduction is observed at approximately 0.43 V versus RHE and agrees well with literature values [13, 33, 41–43]. In contrast, the reduction of Cu(I) to Cu(0) extends over a broad potential range from approximately 0.25 to −0.6 V versus RHE, partly shifted to more negative potentials than the narrower Cu(I) reduction ranges reported in the literature [13, 33, 42–44]. This broad feature may result from surface rearrangement, mixed oxidation states within the reconstructed oxide layer, and transport limitations within the porous electrode structure. In addition, the p-type semiconducting nature of Cu_2O can create a Schottky barrier that requires substantial overpotentials for reduction back to Cu(0) [30], while the rapidly increasing hydrogen evolution reaction (HER) current further overlaps with the Cu(I) reduction signal. Overall, the CV data are consistent with a potential-dependent activation sequence from Cu(0) via Cu(I)- and Cu(II)-containing states toward Cu(III)-containing species under anodic MOR conditions.

The mechanistic relevance of the different Cu oxidation states is further supported by the time-resolved anode potential and product concentration profiles (Figure 4a–c). To follow the surface evolution over consecutive runs, these measurements were conducted using a single foam electrode per composition, and two consecutive experiments are shown. The initial 4.5 min period corresponds to the stepwise current ramp to the target current density, meaning that both the early potential response and the absolute formate production rate are influenced by the increasing applied current.

During the first experiment with the untreated Cu foam (Figure 4a, dotted lines), the formate concentration remained close to zero for the first 3 min, while the anode potential increased through the potential range in which Cu oxidation toward Cu(I)- and Cu(II)-containing surface species is expected. Although the target current density had not yet been reached, a short intermediate feature appeared at approximately 0.7 V versus RHE. This potential is close to the Cu(II)-related oxidation feature observed in the CV measurements and agrees with literature reports for Cu(II) formation on Cu electrodes in alkaline media [13, 30, 33]. We therefore assign this short-lived feature to the onset of Cu(II)-containing surface species during the early oxidative activation of the untreated Cu foam. However, this transition was not resolved as a pronounced plateau because it coincides with the current ramp and is therefore partially masked by the simultaneously increasing applied current. In addition, the Cu(I)-related oxidation feature was only weakly pronounced in the CV measurements (Figure 3). The initially lower surface area of the untreated foam further reduces the charge required for oxidative conversion of the accessible Cu surface, thereby compressing the Cu(II)-related potential region and increasing its overlap with the subsequent oxidation toward Cu(III)-containing species.

Subsequently, the formate concentration began to increase, indicating that Cu(II)-containing surfaces are already more active for MOR to formate than Cu(I)-dominated surfaces, consistent with

21960216, 2026, 22, Downloaded from https://chemistry-europe.onlinelibrary.wiley.com/doi/10.1002/celc.70343 by Universitatsbibliothek RWTH Aachen University, Wiley Online Library on [09/11/2026]. See the Terms and Conditions (https://onlinelibrary.wiley.com/terms-and-conditions) on Wiley Online Library for rules of use; OA articles are governed by the applicable Creative Commons License

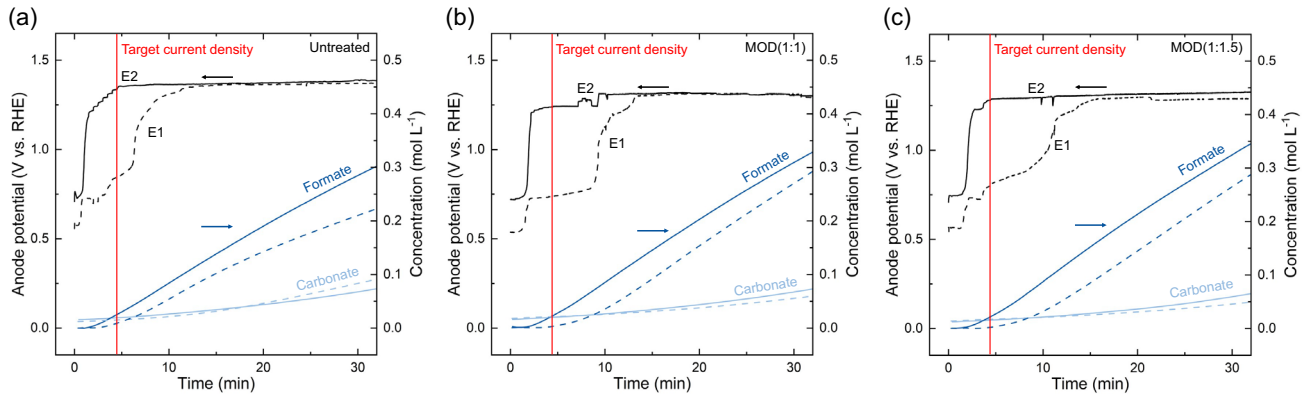


FIGURE 4 | Time-resolved anode potential and product concentration profiles during MOR in the zero-gap flow cell at 200 mA cm^{-2} in 1 M KOH with 1 M methanol at 50 °C for (a) untreated, (b) MOD(1:1), and (c) MOD(1:1.5) Cu foams. Black traces show the anode potential (left axis); blue traces show the concentrations of formate and carbonate determined by in situ FTIR (right axis). Dashed and solid traces denote the first and second consecutive experiments, respectively.

Pawar et al. [45]. The potential then increased further and reached 1.37 V versus RHE after approximately 15 min, which lies within the potential range associated with Cu(II)/Cu(III) transitions. This assignment is supported by the broad anodic feature between approximately 0.8 and 1.7 V versus RHE in the CV measurements and by literature reports for Cu(III)-related species [13, 33, 41–43]. The corresponding formate production rate, calculated from the concentration profiles (Figure S11a), reached its maximum once the final anode potential plateau was established. Together with the CV assignment, this temporal correlation supports the interpretation that increasing formation of Cu(III)-containing species contributes to the highest formate production rate while not constituting direct spectroscopic identification of Cu(III) in the present MOR system.

In the second experiment with the untreated Cu foam (Figure 4a, solid lines), the anode potential moved toward the potential range associated with Cu(II)/Cu(III) transitions already during the current ramp, without a clearly resolved preceding Cu(I)-to-Cu(II) activation region. This behavior shows that the electrode is now activated, starting from a reconstructed Cu oxide/hydroxide interface, most likely dominated by Cu(II)-containing species after removal of the applied potential. Since Cu(III)-containing species are not expected to persist after the potential has been removed [39], the active Cu(III)-containing state is expected to be reestablished during the second anodic polarization. However, this reactivation occurred from a preformed Cu(II)-containing interface rather than from pristine Cu(0), so no separate activation plateau was resolved. Consequently, formate formation started approximately 3 min earlier than in the first experiment, and the formate production rate increased from the beginning of the experiment (Figure S11a). Carbonate formation was less pronounced than during the first experiment, consistent with the higher formate FE of the second untreated run (Figure S12a).

The MOD Cu foams followed the same general activation sequence, but the intermediate Cu(II)-related potential regions were more clearly resolved during the first experiment (Figure 4b,c). For MOD(1:1) and MOD(1:1.5), these regions appeared at approximately 0.73 to 0.78 V versus RHE and 0.74 to 0.91 V versus RHE, respectively, within or slightly above the Cu(I)-to-Cu(II) transition range derived from CV and the literature. Compared to the untreated foam, this region was more pronounced for the MOD Cu foams, consistent with their larger accessible Cu surface area and the higher charge required for oxidative reconstruction. This extended Cu(II)-related region also explains the delayed onset of formate accumulation during the first MOD experiments.

The subsequent potential increase to approximately 1.30 V versus RHE for MOD(1:1) and 1.32 V versus RHE for MOD(1:1.5) placed both MOD Cu foams within the potential range associated with Cu(II)/Cu(III) transitions, where efficient formate production was established. The formate production rates in Figure S11b,c confirm that the MOD Cu foams followed the same activation sequence as the untreated foam, with maxima reached only after the final anode potential had been established during the first experiment. In subsequent experiments, the production rates increased earlier, consistent with faster reactivation of the already reconstructed Cu(II)-containing interface. Once activated, the MOD Cu foams showed rapid formate accumulation with comparatively low carbonate formation.

Overall, the combined potential and concentration profiles show that efficient MOR to formate is established after the formation of a reconstructed Cu(II)-rich interface and after the anode reaches potentials at which Cu(III)-containing species are expected to form. The lower thermodynamic equilibrium potential of MOR compared to OER cannot be fully exploited on Cu-based anodes: The operating potential is governed by the formation and maintenance of the active Cu oxide/oxyhydroxide interface. The untreated foam shows the strongest activation effect between the first and subsequent experiments, whereas the MOD Cu foams display a more controlled activation behavior and maintain lower carbonate formation relative to formate. This supports the interpretation that the MOD-derived microstructure facilitates the formation of an accessible and selective Cu oxide/oxyhydroxide interface under operating conditions.

With the reconstructed operating interface established, we next used the apparent mass-normalized double-layer capacitance, $C_{\mathrm{Dl,m}}$, as a relative proxy for ECSA before and after MOR. Figure 5 summarizes $C_{\mathrm{Dl,m}}$ (Figure 5a) and the corresponding formate FE values at defined methanol conversions used for the performance comparison (Figure 5b).

21960216, 2026, 22, Downloaded from https://chemistry-europe.onlinelibrary.wiley.com/doi/10.1002/celc.70343 by Universitatsbibliothek RWTH Aachen University, Wiley Online Library on [09/11/2026]. See the Terms and Conditions (https://onlinelibrary.wiley.com/terms-and-conditions) on Wiley Online Library for rules of use; OA articles are governed by the applicable Creative Commons License

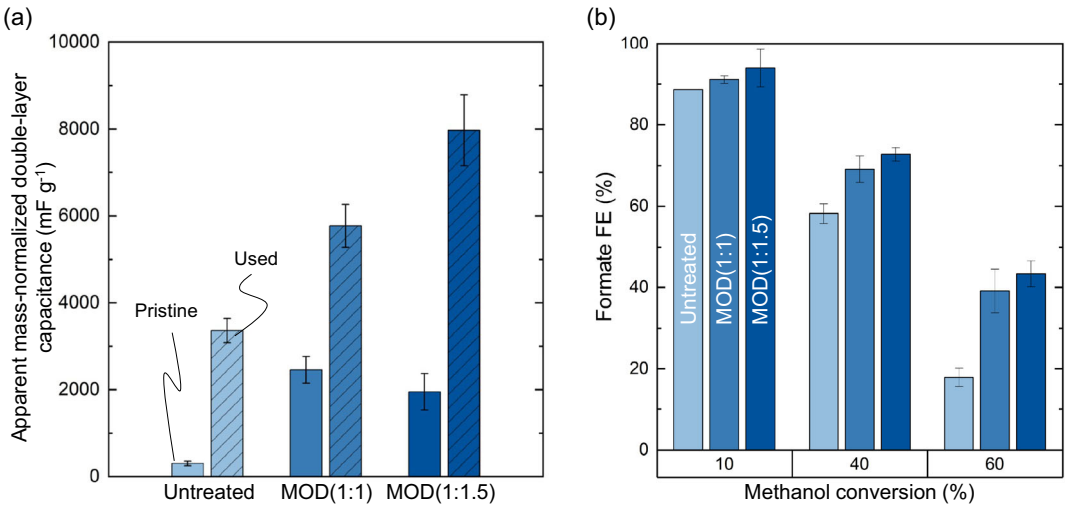


FIGURE 5 | (a) Apparent mass-normalized double-layer capacitance $C_{Dl,m}$ determined for pristine and used Cu foams (untreated, MOD(1:1), and MOD(1:1.5)) in 1 M KOH at room temperature. The pristine MOD values were obtained from two independently prepared electrodes, while the used values were obtained after MOR. (b) Formate FE as a function of methanol conversion at 10%, 40%, and 60% for untreated, MOD(1:1), and MOD(1:1.5) Cu foams at 200 mA cm^{-2} in 1 M KOH containing 1 M methanol at 50 °C. For the FE comparison, the average of the second and third experiments is shown for the untreated Cu foam, while the average of the first and second experiments is shown for the MOD Cu foams.

The $C_{Dl,m}$ values were determined for untreated and MOD Cu foams before and after electrolysis. The scan-rate-dependent regressions are shown in Figures S16–S18, and the resulting values are shown in Table S5. Before electrolysis, the untreated Cu foam exhibited a $C_{Dl,m}$ of 303 mF g^{-1}, whereas MOD(1:1) and MOD(1:1.5) already reached 2456 and 1954 mF g^{-1}, respectively, consistent with their granular morphology compared to the untreated Cu foam (Figure 2). After MOR, $C_{Dl,m}$ increased for all Cu foams, reaching 3362 mF g^{-1} for the untreated Cu foam (+1008%), 5769 mF g^{-1} for MOD(1:1) (+135%), and 7969 mF g^{-1} for MOD(1:1.5) (+308%). The larger relative increase of the untreated Cu foam reflects its initially smooth, low-surface-area state. In contrast, the MOD Cu foams already possessed rough Cu coatings before electrolysis and therefore showed smaller relative gains. Nevertheless, their substantially higher absolute post-MOR $C_{Dl,m}$ values, especially for MOD(1:1.5), are consistent with the MOD-derived microstructure continuing to influence the capacitance response after electrochemical reconstruction.

Because the post-MOR SEM and XRD results above show that all foams reconstruct into Cu(II)-containing sheet-like interfaces, the post-MOR $C_{Dl,m}$ values are taken as the most representative descriptor of the catalytically relevant interface under steady-state operation. Importantly, the increase in $C_{Dl,m}$ after MOR cannot be ascribed solely to surface-area enlargement. The formation of Cu(II)-containing flakes roughens the electrode surface and generates a nanostructured oxide overlayer, thereby increasing the accessible electrode–electrolyte interface and the density of electrochemically addressable sites [31]. At the same time, Cu(II)/CuO phases are themselves electrochemically active and can contribute to redox-derived pseudocapacitance [46, 47]. The measured $C_{Dl,m}$ therefore reflects the combined effect of morphological reconstruction and the intrinsically pseudocapacitive character of the Cu(II)-containing interface. However, since comparable sheet-like reconstruction products formed on all foams, the higher post-MOR $C_{Dl,m}$ values of the MOD Cu foams are interpreted as a relative indication of a larger ECSA associated with the MOD-derived microstructure, while recognizing the contribution of pseudocapacitance.

To evaluate how the relative ECSA proxy, $C_{Dl,m}$, relates to catalytic performance, the formate FE was extracted from the continuous FE–conversion profiles at defined methanol conversions of 10%, 40%, and 60% (Figure 5b). This pointwise representation enables a direct comparison of the catalyst performance at early, intermediate, and high methanol conversion, while the corresponding FE–conversion profiles and continuous concentration data are shown in Figures S12–S15.

Reproducibility was first assessed by performing three consecutive MOR experiments on an untreated Cu foam (Figure S12a). The first experiment showed distinctly different behavior, with a lower formate FE at low methanol conversion, a more pronounced decline in FE, and a different overall FE–conversion profile compared to the subsequent experiments. In contrast, the second and third experiments were highly reproducible and followed nearly identical FE–conversion curves. This difference indicates that the pristine untreated Cu foam underwent an initial activation and surface reconstruction during the first operation period, whereas a more stable catalytic state was established thereafter. Therefore, the second and third experiments were used for the untreated Cu foam in the comparative evaluation.

For the MOD Cu foams, the differences between consecutive experiments were less pronounced but not absent. This becomes apparent in the time-resolved concentration profiles shown in Figures S13–S15. The first experiment generally showed a delayed increase in formate concentration, consistent with the initial oxidative reconstruction of the MOD-derived Cu surface discussed above. After this activation period, formate accumulated and reached a slightly higher maximum concentration, while carbonate formation was delayed compared to subsequent experiments. In the following runs, formate formation started earlier, indicating that the catalytically relevant oxidized interface had already been

21960216, 2026, 22, Downloaded from https://chemistry-europe.onlinelibrary.wiley.com/doi/10.1002/celc.70343 by Universitatsbibliothek RWTH Aachen University, Wiley Online Library on [09/11/2026]. See the Terms and Conditions (https://onlinelibrary.wiley.com/terms-and-conditions) on Wiley Online Library for rules of use; OA articles are governed by the applicable Creative Commons License

established during the first experiment. However, these later experiments also showed an earlier increase in carbonate concentration and a slightly lower maximum formate concentration. The methanol concentration profiles remained nearly parallel between consecutive experiments, indicating that the observed differences mainly arise from changes in selectivity and surface state rather than from differences in methanol availability. Importantly, the first and second MOD experiments showed substantially smaller deviations in the FE–conversion profiles than observed between the first and subsequent experiments of the untreated Cu foam, as shown for MOD(1:1) and MOD(1:1.5) in Figure S12b,c, respectively. Therefore, the first and second experiments were used for the comparative evaluation of the MOD Cu foams. This choice is further supported by additional MOD(1:1) experiments from an independent series with a second set of electrodes, where the second and third runs closely followed the second run of the first series, indicating reproducible performance after the initial surface reconstruction (Figures S13b–S15b). Across the investigated consecutive runs, no progressive deterioration was observed after the initial surface reconstruction. For the untreated Cu foam, the nearly identical second and third FE–conversion profiles further support the reproducibility of the reconstructed catalytic state (Figure S12a). These experiments therefore demonstrate reproducibility over the investigated runs but do not constitute a long-term durability assessment under constant electrolyte composition.

The resulting pointwise FE comparison shows that all electrodes exhibited high formate FEs at low methanol conversion, but that the performance differences became increasingly pronounced with increasing conversion. At 10% methanol conversion, the untreated Cu foam reached a formate FE of 88.6%, while MOD(1:1) and MOD(1:1.5) reached 91.1% and 93.9%, respectively. At 40% conversion, the untreated Cu foam retained only 58.2% formate FE, whereas MOD(1:1) and MOD(1:1.5) maintained higher values of 69.1% and 72.7%, respectively. This trend became most pronounced at 60% conversion, where the formate FE decreased to 17.9% for the untreated Cu foam but remained substantially higher for MOD(1:1) and MOD(1:1.5), reaching 39.1% and 43.3%, respectively. The corresponding standard deviations are shown as error bars in Figure 5b.

These performance trends broadly follow the post-experiment $C_{Dl,m}$ values, which are used here as a relative proxy for ECSA. However, the improved MOR performance cannot be attributed to ECSA alone. XRD and XPS show that the MOD electrodes reconstruct toward oxidized Cu(II)-rich surface states under MOR conditions, which may influence the formation and availability of high-valent Cu species under anodic polarization. Because the additional EDX and XPS analyses were performed only for the MOD electrodes, these measurements do not establish a distinct surface chemical state of the MOD electrodes relative to the untreated Cu foam as the origin of the observed performance difference. Mass transport within porous electrodes may additionally influence local reactant and product concentrations, but the present measurements do not independently resolve such a contribution. The differences between the electrodes become particularly pronounced at higher methanol conversion, where the untreated Cu foam shows a strong decrease in formate FE, whereas the MOD Cu foams maintain substantially higher selectivity. This observation underscores the importance of evaluation at high conversions.

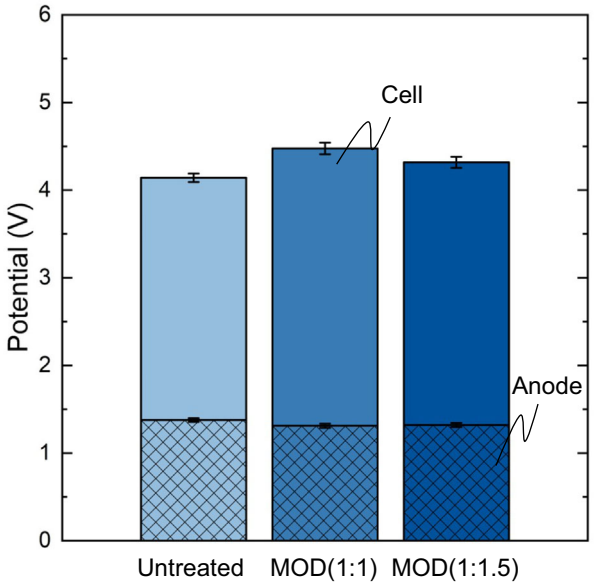


FIGURE 6 | Anode and cell potentials measured during methanol oxidation in 1 M KOH containing 1 M methanol at 200 mA cm^{-2} and 50 °C for untreated, MOD(1:1), and MOD(1:1.5) Cu foam electrodes. An RHE served as the reference electrode. For the untreated Cu foam, the second and third experiments are shown; for the MOD Cu foams, the first and second experiments are shown. Error bars indicate the variation between repeated measurements.

In addition, the MOD Cu foams enabled higher final methanol conversions, increasing from 64.0% for the untreated Cu foam to 70.4% for MOD(1:1) and 72.2% for MOD(1:1.5).

Finally, the cell and anode potentials were examined to determine whether the improved selectivity and conversion of the MOD Cu foams were accompanied by systematic changes in the voltage response under galvanostatic flow cell operation (Figure 6).

The overall cell potentials were similar for all foams, remaining within 4.3 ± 0.2 V. Minor differences in absolute cell voltage should be interpreted with caution because the cell voltage includes contributions from the thermodynamic equilibrium potential, anodic and cathodic overpotentials, membrane resistance, and electrolyte resistance. Moreover, the untreated Cu foam was tested with a fresh bipolar membrane (BPM), whereas the same BPM was reused for the MOD Cu foam experiments. The slightly higher cell voltages observed for the MOD Cu foams, particularly for MOD(1:1), are therefore likely affected by membrane aging rather than intrinsic anode differences. Accordingly, the improved performance of the MOD Cu foams is reflected mainly in enhanced formate selectivity and higher methanol conversion, not in a lower cell potential. The anode potential did not increase for the MOD Cu foams but rather showed a slight decrease, consistent with lower effective local current densities at the Cu interface.

3 | Conclusion

In this work, we demonstrate that Cu-based MOD inks provide an effective route to engineer structured Cu foam electrodes for

21960216, 2026, 22, Downloaded from https://chemistry-europe.onlinelibrary.wiley.com/doi/10.1002/celc.70343 by Universitatsbibliothek RWTH Aachen University, Wiley Online Library on [09/11/2026]. See the Terms and Conditions (https://onlinelibrary.wiley.com/terms-and-conditions) on Wiley Online Library for rules of use; OA articles are governed by the applicable Creative Commons License

the MOR to formate. The MOD ink approach provides a solution-based coating route for complex porous Cu foams, with granular coating structures observed both at the outer surface and in the cross-sectional regions examined. By tuning the molar ratio of Cu(II) formate tetrahydrate to MIPA, the morphology of the resulting Cu coatings could be systematically adjusted. In particular, the MOD(1:1.5) formulation reduced the apparent Cu cluster size to below 1 μm and yielded the highest post-operation $C_{Dl,m}$ value.

Electrochemical and structural analyses show that the Cu surface undergoes rapid reconstruction under MOR conditions, forming oxidized Cu species. Together with the CV and time-resolved potential response, this behavior is consistent with the transient formation of Cu(III)-containing species under anodic polarization, which are implicated as catalytically relevant oxidizing species for formate production. This surface evolution is accompanied by a substantial increase in the apparent mass-normalized double-layer capacitance, $C_{Dl,m}$, which is used here as a relative proxy for ECSA. The untreated Cu foam exhibited a mass-normalized double-layer capacitance of only 303 mF g^{-1} prior to electrolysis, whereas MOD(1:1) and MOD(1:1.5) already reached 2456 and 1954 mF g^{-1}, respectively. After electrolysis, the capacitance increased further, with MOD(1:1.5) reaching the highest value of 7969 mF g^{-1}. These post-electrolysis apparent mass-normalized double-layer capacitance trends broadly follow the catalytic performance, indicating that the catalytically relevant interface is established during the initial activation period and remains strongly influenced by the MOD-derived microstructure.

Consistent with this behavior, the MOD Cu foams outperform the untreated foam in both selectivity and methanol conversion. At 10% methanol conversion, the best-performing MOD(1:1.5) Cu foam achieved a formate FE of 93.9%, compared to 88.6% for untreated Cu foam. More importantly, the improvement became increasingly pronounced at higher conversion, where MOD(1:1.5) maintained a formate FE of 43.3% at 60% methanol conversion, compared to only 17.9% for untreated Cu foam. The final methanol conversion increased from 64.0% for untreated Cu foam to 72.2% for MOD(1:1.5). These results indicate that the higher $C_{Dl,m}$ values, used here as a relative proxy for ECSA, are associated with the improved catalytic performance. The reconstructed Cu surface chemistry may additionally contribute to the observed behavior. However, the present chemical characterization does not independently establish surface-state differences between the untreated and MOD Cu foams. Additional mass-transport contributions also cannot be independently resolved in the present study.

Overall, this work establishes MOD inks as a versatile platform for the fabrication of structured electrocatalysts on porous metallic substrates. Beyond their original use in printed electronics, MOD inks can therefore be repurposed as scalable catalyst-coating precursors for electrochemical synthesis. More broadly, the ability to tune cluster size, catalyst distribution, and surface morphology within complex three-dimensional electrodes opens new opportunities for the design of advanced catalytic architectures for selective liquid-phase electrosynthesis.

Future studies should clarify whether residual carbon-containing surface species originating from the MOD processing influence MOR activity and formate selectivity, and how these species evolve under electrochemical operating conditions.

4 | Experimental Section

4.1 | Preparation of Metal–Organic Decomposition Cu Foams

MOD Cu foams were prepared according to the four-step workflow shown in Figure 1. In step 1, the Cu foam substrate (50 pores per inch (ppi), 4 mm thickness; Recemat BV) was cut into the required electrode geometry. To obtain one 6 cm × 6 cm Cu foam electrode, two 3 cm × 6 cm pieces were prepared due to geometric restrictions of the tubular oven (STF 16/610, Carbolite) used for calcination. The Cu foam pieces were ultrasonically cleaned in acetone for 15 min, rinsed with deionized water, and dried in air.

In step 2, the Cu-based MOD ink was synthesized following the procedure reported by Huang et al. [22]. In a typical synthesis, 0.07 mol of Cu(II) formate tetrahydrate was added to MIPA. The molar ratio of Cu(II) formate tetrahydrate to MIPA was systematically varied (1:1, 1:1.5, and 1:2). The mixtures were magnetically stirred at 300 rpm for at least 1 h to ensure complete dissolution and homogenization. In addition, two modified 1:1 inks were prepared: In one formulation, octylamine (OA) was introduced as a co-ligand at a Cu(II) formate tetrahydrate: MIPA:OA molar ratio of 1:1:1, while in a second formulation, 1 wt% PVP was added to the 1:1 MOD ink. The pretreated Cu foam pieces from step 1 were then fully immersed in the freshly prepared MOD ink and ultrasonicated for 30 min to promote the infiltration of the molecular precursor into the porous scaffold.

In step 3, thermal decomposition of the deposited precursor was carried out in a tubular oven under a constant argon flow of 400 mL min^{-1}. Samples were heated at a rate of 5 °C min^{-1} to 138 °C, held for 90 min, and subsequently cooled to room temperature under argon.

In step 4, the coated electrodes were cleaned by repeated ultrasonication in fresh isopropanol for 5 min to remove occasionally observed yellowish or brown surface discoloration, likely originating from residual MIPA or organic decomposition products. The cleaning procedure was repeated until no further discoloration was observed.

4.2 | Electrochemical Methanol Oxidation in a Flow Cell

MOR experiments were performed in a zero-gap flow cell (flex-E-cell, FXC) equipped with a BPM and metal foam electrodes (Figure S19). Untreated or MOD Cu foams were used as the anode, with a total geometric area of 6 cm × 6 cm and an overall thickness of 4 mm. Due to spatial constraints imposed by the tubular oven, the MOD Cu foams were assembled from two separate Cu foam pieces (each 3 cm × 6 cm), which were placed adjacent to each other to achieve the required total geometric area. The untreated Cu foam did not require calcination in the tubular oven and was therefore used as a single piece cut

21960216, 2026, 22, Downloaded from https://chemistry-europe.onlinelibrary.wiley.com/doi/10.1002/celc.70343 by Universitatsbibliothek RWTH Aachen University, Wiley Online Library on [09/11/2026]. See the Terms and Conditions (https://onlinelibrary.wiley.com/terms-and-conditions) on Wiley Online Library for rules of use; OA articles are governed by the applicable Creative Commons License

directly to 6 cm × 6 cm. The cathode was a 5 cm × 6 cm Ag foam (areal density 5500 g m^{-2}, Alantum), etched in 30 % HNO_3 for 10 s following Zhang et al. [48, 49] to increase the surface area. To define a total active area of 5 cm × 5 cm for both electrodes, a 0.1 mm ethylene tetrafluoroethylene (ETFE) gasket with a 5 cm × 5 cm cutout was placed on each electrode. Anode and cathode compartments were separated by a Weifang BPM (Weifang Senya Chemical Co., Ltd.).

The anolyte consisted of 1 M KOH and 1 M methanol, with a total volume ranging from 57 to 62 mL, depending on the specific anode configuration. Prior to each experiment, only the anolyte tubing was filled with the required electrolyte volume in order to keep the total anolyte volume as low as possible. During operation, the anolyte was circulated through this closed loop at 100 mL min^{-1}. The total volume of the anolyte tubing was determined for one anode configuration. For each new anode, the effective anolyte volume was recalculated based on the anode mass and the density of the Cu foam, accounting for variations in the volume displaced by the electrode material. This procedure ensured accurate determination and control of the electrolyte volume for all measurements. The catholyte consisted of 3 M potassium bicarbonate. It was recirculated at 100 mL min^{-1} and continuously replenished with fresh electrolyte at 4 mL min^{-1} to maintain a stable composition during CO_2R, following the feed-and-bleed setup reported by Baessler et al. [50]. Both electrolytes were circulated through a heat exchanger and maintained at 50 °C. A detailed flowsheet of the experimental setup is shown in Figure S20. Galvanostatic operation was conducted using a BioLogic SP-150 potentiostat equipped with a booster. To reduce stress on the BPM, the current density was increased stepwise by 20 mA cm^{-2} every 30 s until reaching a final current density of 200 mA cm^{-2}. The current was switched off once the formate concentration reached its maximum, corresponding to a formate FE of 0%. To record the anode potential, a RHE (Mini-HydroFlex, Gaskatel) was used as a reference electrode positioned at the anolyte inlet of the electrochemical cell.

4.3 | Product Analysis and Evaluation

The anodic liquid products were continuously monitored in situ by Fourier transform infrared (FTIR) spectroscopy (ReactIR 702L with micro flow cell, Mettler Toledo) every 30 s. The FTIR was calibrated for the substrate methanol and KOH, the product formate, and the side product carbonate. The continuous concentration profiles obtained from FTIR were used to calculate the formate FE according to Equation (1), with z denoting the number of transferred electrons, F the Faraday constant, V the respective anolyte volume depending on the anode used, I the applied current, c the concentration at the measured time point n, and t the time at the measured time point n.

$$\mathrm{FE}_n = \frac{z \cdot F \cdot V}{I} \cdot \frac{c_{n+1} - c_{n-1}}{t_{n+1} - t_{n-1}} \tag{1}$$

Methanol conversion was calculated according to Equation (2), with $c_{\mathrm{MeOH},0}$ denoting the initial methanol concentration at the beginning of the experiment and $c_{\mathrm{MeOH},n}$ the concentration of methanol at time n.

$$\mathrm{conversion}_n = \frac{c_{\mathrm{MeOH},0} - c_{\mathrm{MeOH},n}}{c_{\mathrm{MeOH},0}} \tag{2}$$

For subsequent evaluation, the formate FE was analyzed as a function of methanol conversion. This representation enables a more complete assessment of catalyst performance because MOR selectivity changes during electrolysis as methanol is consumed, products accumulate, and the electrolyte composition evolves. Therefore, comparing the formate FE at defined conversion levels provides a more meaningful evaluation than considering only the initial selectivity. The relatively small anolyte volume (57 to 62 mL) and the active electrode area of 25 cm^2 allowed early-, intermediate-, and high-conversion regimes to be accessed within a single experiment. Similar conversion-dependent changes in formate FE during MOR have been reported by Baessler et al. [5]. Owing to the initial ramp-up phase (4.5 min), during which the current density was increased stepwise to the target value, together with the finite response time of the continuous FTIR analysis, FE values obtained at very low methanol conversion were excluded from further evaluation.

4.4 | Apparent Mass-Normalized Double-Layer Capacitance Measurements

To assess relative differences in ECSA, the apparent mass-normalized double-layer capacitance, $C_{\mathrm{Dl,m}}$, was determined by scan-rate-dependent CV in an undivided beaker containing 1 M KOH at room temperature using a three-electrode configuration. The investigated electrode was cut to dimensions of 3 cm × 1 cm and served as the working electrode. Electrical contact was established at the upper edge using a clamp, while the remaining area was masked with chemically resistant adhesive tape to define a geometric electrode area of 1 cm^2. A Ni foam (grade 4753, Recemat NL) with dimensions of approximately 6 cm × 6 cm was used as the counter electrode, and a RHE (Mini-HydroFlex, Gaskatel) was used as the reference electrode. Prior to each measurement series, the uncompensated resistance was determined by potentiostatic electrochemical impedance spectroscopy (PEIS) under open-circuit conditions. The impedance spectra were recorded at 0 V between the working and counter electrode over a frequency range from 400 kHz to 5 Hz using a sinusoidal excitation amplitude of 5 mV. The electrolyte resistance was obtained from the high-frequency intercept with the real axis in the Nyquist plot, and 85% iR compensation was applied. Before the scan-rate-dependent measurements, the electrodes were preconditioned by CV in the potential range from 1.30 to 1.40 V versus RHE at a scan rate of 2 mV s^{-1} until a stable voltammetric response was obtained and no significant deviations between consecutive cycles were observed. Subsequently, cyclic voltammograms were recorded in the same potential range at scan rates of 2, 4, 6, 8, and 10 mV s^{-1}. Five cycles were recorded at each scan rate, and only the final cycle was used for analysis. The anodic and cathodic capacitive current was extracted at 1.35 V versus RHE and plotted as a function of the scan rate. Applying a linear fit yielded C_{Dl}, which was then normalized to the electrode mass to obtain $C_{\mathrm{Dl,m}}$. In the present work, $C_{\mathrm{Dl,m}}$ is used as a relative proxy for ECSA rather than being converted into an absolute ECSA value, since conversion by a single material-specific capacitance value can introduce substantial uncertainty [51].

21960216, 2026, 22, Downloaded from https://chemistry-europe.onlinelibrary.wiley.com/doi/10.1002/celc.70343 by Universitatsbibliothek RWTH Aachen University, Wiley Online Library on [09/11/2026]. See the Terms and Conditions (https://onlinelibrary.wiley.com/terms-and-conditions) on Wiley Online Library for rules of use; OA articles are governed by the applicable Creative Commons License

4.5 | Cyclic Voltammetry Measurements

CV measurements were carried out in the same undivided beaker cell and under otherwise identical conditions as used for the $C_{Dl,m}$ determination, including room-temperature operation, PEIS-based iR compensation, identical electrical contacting of the Cu foam working electrodes, and the same Ni foam counter electrode (approximately 6 cm × 6 cm) and RHE (Mini-HydroFlex, Gaskatel) as the reference electrode. Unlike the scan-rate-dependent measurements in the non-Faradaic region, CVs were recorded in 1 M KOH and in 1 M KOH containing 1 M methanol over a wider potential range from −0.9 to 1.9 V versus RHE at a fixed scan rate of 20 mV s^{-1}. For each electrolyte, five consecutive cycles were recorded, and only the final cycle was used for evaluation.

4.6 | X-Ray Diffraction Measurements

XRD measurements were carried out ex situ using a Malvern Panalytical Empyrean II diffractometer equipped with a Cu anode source (Empyrean Cu LFF HR) operated at 40 kV and 40 mA. A 10-mm area mask, a 0.125° divergence slit, and 0.04° Soller slits on both the incident and diffracted beam sides were used. Cu Kβ radiation was suppressed using a 0.02 mm Ni filter. Diffraction patterns were recorded in ω–2θ geometry over a 2θ range from 5° to 130° using a PIXcel 3D detector positioned 240 mm from the sample. Data were collected with an angular resolution of approximately 0.026° and an effective integration time of 150 s. For data processing, the background was estimated by morphology-inspired baseline extraction using a one-dimensional minimum filter (window size: 1000 points), which captures the slowly varying lower envelope of the diffraction pattern. This baseline was subsequently subtracted from the experimental data, and negative intensity values were truncated to zero.

Acknowledgments

M. Wessling acknowledges DFG funding through the Gottfried Wilhelm Leibniz Award 2019 (WE 4678/12-1). This work was conducted in part at the Competence Center for Industrial Electrochemistry ELECTRA, which is supported by the European Regional Development Fund (ERDF) and the Federal State of North Rhine-Westphalia (grant no. ERDF 05 00 07 7). This work was funded by the Federal State of North Rhine-Westphalia as part of the project Air2chem (EFRE-20800379). This work was supported by the German Federal Ministry of Education and Research (BMBF) within the project iNEW 2.0 (FKZ 03SF0627). During the preparation of this workup to August 19, 2026, the authors used ChatGPT (GPT-5.6) and OpenAI Codex to improve manuscript readability and to support the generation of Python code for processing and evaluating experimental data. The tools were used for language editing throughout the manuscript and for coding data-processing routines based on predefined calculation procedures. All outputs were reviewed and verified by the authors, who take full responsibility for the content of the publication.

Open Access funding enabled and organized by Projekt DEAL.

Funding

This study was supported by Gottfried Wilhelm Leibniz Award 2019 (WE 4678/12-1), European Regional Development Fund (ELECTRA (ERDF 05 00 07 7), Air2chem (EFRE-20800379)), and Bundesministerium für Bildung und Forschung (iNEW 2.0, FKZ 03SF0627).

Conflicts of Interest

The authors declare no conflicts of interest.

Data Availability Statement

The data that support the findings of this study are openly available in Zenodo at https://doi.org/10.5281/zenodo.22010537, reference number 22010537.

References

1. S. Liu, B. Tian, X. Xu, et al., "Ampere-Level Electrolytic Coproduction of Formate with Coupled Carbon Dioxide Reduction and Selective Methanol Oxidation," *ACS Catalysis* 14 (2024): 9476.

2. W. Xi, P. Yang, M. Jiang, et al., "Electrochemical CO_2 Reduction Coupled with Alternative Oxidation Reactions: Electrocatalysts, Electrolytes, and Electrolyzers," *Applied Catalysis B: Environmental* 341 (2024): 123291.

3. X. Wei, Y. Li, L. Chen, and J. Shi, "Formic Acid Electro-Synthesis by Concurrent Cathodic CO_2 Reduction and Anodic CH_3 OH Oxidation," *Angewandte Chemie International Edition* 60 (2021): 3148.

4. Y. Zhou, Z. Wang, W. Fang, et al., "Modulating O–H Activation of Methanol Oxidation on Nickel-Organic Frameworks for Overall CO_2 Electrolysis," *ACS Catalysis* 13 (2023): 2039.

5. J. Baessler, N. Vollmert, J. Vehrenberg, et al., "Reaction Engineering for High Yield Electrosynthesis: Unraveling the Impact of Reaction Conditions and Conversion on Methanol Oxidation to Formate," *Chemical Engineering Journal* 495 (2024): 153000.

6. H. Xu, Y. Xu, Q. Zhang, Q. Zhang, J. Liu, and H. Bian, "Methanol Oxidation Reaction-Assisted Cu_2 O/CuO with Enhanced Electrochemical Performance for Water Splitting," *European Journal of Inorganic Chemistry* 28 (2025): e202500095.

7. IMARC Group, "Formic Acid Market: Global Industry Trends, Share, Size, Growth, Opportunity and Forecast," 2026.

8. Chemanalyst, "Formic Acid Price Trend and Forecast," 2026.

9. Chemanalyst, "Methanol Price Trend and Forecast," 2026.

10. L. Hou, C. Sun, Z. Zhang, X. Liu, and J. Cho, "Methanol Electrochemical Upgrading to Formate for Energy Applications," *Small* 21 (2025): 2505525.

11. B. D. Queiroz, P.-L. S. Vital, K. O. Budke, et al., "A Comprehensive Investigation of Methanol Electrooxidation on Copper Anodes: Spectroelectrochemical Insights and Energy Conversion in Microfluidic Fuel Cells," *ACS Applied Materials & Interfaces* 16 (2024): 35255.

12. J. Li, H. Yu, J. Na, et al., "Recent Advances in Selective Methanol Oxidation Electrocatalysts for the Co-Production of Hydrogen and Value-Added Formate," *Catalysis Science & Technology* 14 (2024): 5525.

13. Z. Shaghaghi, R. Bikas, M. Aligholivand, S. Jafari, and V. Kinzhybalo, "Enhanced Methanol Electro-Oxidation Activity of CuO Nanoparticles Derived from the Thermal Decomposition of a CuII Salophen Type Coordination Compound," *Scientific Reports* 15 (2025): 4394.

14. S. Sakong and A. Gross, "Total Oxidation of Methanol on Cu(110): a Density Functional Theory Study," *The Journal of Physical Chemistry A* 111 (2007): 8814.

15. D. M. Heard and A. J. J. Lennox, "Electrode Materials in Modern Organic Electrochemistry," *Angewandte Chemie (International Edition, in English)* 59 (2020): 18866.

16. T. N. Huan, G. Rousse, S. Zanna, et al., "A Dendritic Nanostructured Copper Oxide Electrocatalyst for the Oxygen Evolution Reaction," *Angewandte Chemie International Edition* 56 (2017): 4792.

17. D. Ahmadkhaniha, M. Sieber, and C. Zanella, "Controlling Coating Thickness Distribution for A Complex Geometry with the Help of

21960216, 2026, 22, Downloaded from https://chemistry-europe.onlinelibrary.wiley.com/doi/10.1002/celc.70343 by Universitatsbibliothek RWTH Aachen University, Wiley Online Library on [09/11/2026]. See the Terms and Conditions (https://onlinelibrary.wiley.com/terms-and-conditions) on Wiley Online Library for rules of use; OA articles are governed by the applicable Creative Commons License

Simulation," *The International Journal of Advanced Manufacturing Technology* 134 (2024): 3703.

18. I. Belov, C. Zanella, C. Edström, and P. Leisner, "Finite Element Modeling of Silver Electrodeposition for Evaluation of Thickness Distribution on Complex Geometries," *Materials & Design* 90 (2016): 693.

19. A. J. Kell, K. Wagner, X. Liu, B. H. Lessard, and C. Paquet, "Advanced Applications of Metal–Organic Decomposition Inks in Printed Electronics," *ACS Applied Electronic Materials* 6 (2024): 1.

20. C. Paquet, T. Lacelle, X. Liu, et al., "The Role of Amine Ligands in Governing Film Morphology and Electrical Properties of Copper Films Derived from Copper Formate-Based Molecular Inks," *Nanoscale* 10 (2018): 6911.

21. W. Yang, E. J. W. List-Kratochvil, and C. Wang, "Metal Particle-Free Inks for Printed Flexible Electronics," *Journal of Materials Chemistry C* 7 (2019): 15098.

22. K.-M. Huang, H. Tsukamoto, Y. Yong, et al., "Stabilization of the Thermal Decomposition Process of Self-Reducible Copper Ion Ink for Direct Printed Conductive Patterns," *RSC Advances* 7 (2017): 25095.

23. D.-H. Shin, S. Woo, H. Yem, et al., "A Self-Reducible and Alcohol-Soluble Copper-Based Metal–Organic Decomposition Ink for Printed Electronics," *ACS Applied Materials & Interfaces* 6 (2014): 3312.

24. A. Yabuki, N. Arriffin, and M. Yanase, "Low-Temperature Synthesis of Copper Conductive Film by Thermal Decomposition of Copper–amine Complexes," *Thin Solid Films* 519 (2011): 6530.

25. Y.-H. Choi and S.-H. Hong, "Effect of the Amine Concentration on Phase Evolution and Densification in Printed Films Using Cu(II) Complex Ink," *Langmuir* 31 (2015): 8101.

26. B. Zhang, C. Chen, W. Li, J. Yeom, and K. Suganuma, "Well-Controlled Decomposition of Copper Complex Inks Enabled by Metal Nanowire Networks for Highly Compact, Conductive, and Flexible Copper Films," *Advanced Materials Interfaces* 7 (2020): 1901550.

27. W. Xu, X. Dai, T. Zhang, and T. Wang, "Dual Effects of Water on the Performance of Copper Complex Conductive Inks for Printed Electronics," *Chemical Engineering Science* 190 (2018): 40.

28. Y. Choi, K.-D. Seong, and Y. Piao, "Metal−Organic Decomposition Ink for Printed Electronics," *Advanced Materials Interfaces* 6 (2019): 1901002.

29. J. Choi, S. Park, D. Kim, et al., "Cu Nanoparticle Infiltration via Metal–Organic Decomposition Ink for Superior Mass Activity in CO Electroreduction," *Nano Letters* 25 (2025): 15346.

30. S. T. Mayer and R. H. Muller, "An In Situ Raman Spectroscopy Study of the Anodic Oxidation of Copper in Alkaline Media," *Journal of the Electrochemical Society* 139 (1992): 426.

31. B. K. Singh, A. Shaikh, R. O. Dusane, and S. Parida, "Copper Oxide Nanosheets and Nanowires Grown by One-Step Linear Sweep Voltammetry for Supercapacitor Application," *Journal of Energy Storage* 31 (2020): 101631.

32. H. Heli, M. Jafarian, M. G. Mahjani, and F. Gobal, "Electro-Oxidation of Methanol on Copper in Alkaline Solution," *Electrochimica Acta* 49 (2004): 4999.

33. R. Ojani, J.-B. Raoof, and Y. Ahmady-Khanghah, "Copper-Poly(2-aminodiphenylamine) as a Novel and Low Cost Electrocatalyst for Electrocatalytic Oxidation of Methanol in Alkaline Solution," *Electrochimica Acta* 56 (2011): 3380.

34. C.-X. Zhang, D. Yin, Y.-X. Zhang, et al., "A High-Entropy Oxyhydroxide with a Graded Metal Network Structure for Efficient and Robust Alkaline Overall Water Splitting," *Advanced Science* 11 (2024): 2406008.

35. P. Jiang, D. Prendergast, F. Borondics, et al., "Experimental and Theoretical Investigation of the Electronic Structure of Cu_2O and CuO Thin Films on Cu(110) Using X-Ray Photoelectron and Absorption Spectroscopy," *The Journal of Chemical Physics* 138 (2013): 024704.

36. J. Wang, C. Li, Y. Zhu, J. A. Boscoboinik, and G. Zhou, "Insight into the Phase Transformation Pathways of Copper Oxidation: From Oxygen Chemisorption on the Clean Surface to Multilayer Bulk Oxide Growth," *The Journal of Physical Chemistry C* 122 (2018): 26519.

37. X. Sun, W. Zhu, D. Wu, et al., "Surface-Reaction Induced Structural Oscillations in the Subsurface," *Nature Communications* 11 (2020): 305.

38. D. P. Adiyeri Saseendran, J. W. A. Fischer, L. Müller, et al., "Copper(ii) Defect-Cubane Water Oxidation Electrocatalysts: from Molecular Tetramers to Oxidic Nanostructures," *Chemical Communications* 59 (2023): 5866.

39. J. Lei, H. Zhang, J. Yang, et al., "Structural Designs and Mechanism Insights into Electrocatalytic Oxidation of 5-hydroxymethylfurfural," *Journal of Energy Chemistry* 100 (2025): 792.

40. Y. Deng, A. D. Handoko, Y. Du, S. Xi, and B. S. Yeo, "*In Situ* Raman Spectroscopy of Copper and Copper Oxide Surfaces during Electrochemical Oxygen Evolution Reaction: Identification of Cu^{III} Oxides as Catalytically Active Species," *ACS Catalysis* 6 (2016): 2473.

41. M. R. Othman, Riyanto, "Electrochemical Stability of Cu, Ni, Co, Pt and Ir Metals Sheet and Their Composite Electrodes in Potassium Hydroxide Solution," *International Journal of Electrochemical Science* 7 (2012): 8408.

42. J.-B. He, D.-Y. Lu, and G.-P. Jin, "Potential Dependence of Cuprous/Cupric Duplex Film Growth on Copper Electrode in Alkaline Media," *Applied Surface Science* 253 (2006): 689.

43. A. Khouchaf, D. Takky, M. E. M. Chbihi, and S. Benmokhtar, "Electrocatalytic Oxidation of Methanol on Glassy Carbon Electrode Modified by Metal Ions (Copper and Nickel) Dispersed into Polyaniline Film," *Journal of Materials Science and Chemical Engineering* 04 (2016): 97.

44. U. Collisi and H.-H. Strehblow, "The Formation of Cu_2O Layers on Cu and Their Electrochemical and Photoelectrochemical Properties," *Journal of Electroanalytical Chemistry and Interfacial Electrochemistry* 284 (1990): 385.

45. S. M. Pawar, J. Kim, A. I. Inamdar, et al., "Multi-Functional Reactively-Sputtered Copper Oxide Electrodes for Supercapacitor and Electro-Catalyst in Direct Methanol Fuel Cell Applications," *Scientific Reports* 6 (2016): 21310.

46. E. Espejo and M. D. L. Balela, "Electrochemical Investigation of Cupric Oxide Grown on Copper Foil via Chemical Bath Deposition," *Solid State Phenomena* 266 (2017): 105.

47. T. S. Bhat, A. M. Teli, S. A. Beknalkar, et al., "Activated Carbon Mediated Hydrothermally Synthesized CuO Thin Films for Electrochemical Supercapacitors," *ECS Journal of Solid State Science and Technology* 11 (2022): 063003.

48. Z. Zhang, E. W. Lees, S. Ren, B. A. W. Mowbray, A. Huang, and C. P. Berlinguette, "Conversion of Reactive Carbon Solutions into CO at Low Voltage and High Carbon Efficiency," *ACS Central Science* 8 (2022): 749.

49. Z. Zhang, E. W. Lees, F. Habibzadeh, et al., "Porous Metal Electrodes Enable Efficient Electrolysis of Carbon Capture Solutions," *Energy & Environmental Science* 15 (2022): 705.

50. J. Baessler, M. Wehner, M. Mohseni, J. Neumann, M. Wessling, and R. Keller, "Feed and Bleed Operating Mode for Electrochemical Flow Cells: Challenges, Solutions and Practical Insights," *ChemElectroChem* 12 (2025): e202500034.

51. D. M. Morales and M. Risch, "Seven Steps to Reliable Cyclic Voltammetry Measurements for the Determination of Double Layer Capacitance," *Journal of Physics: Energy* 3 (2021): 034013.

Supporting Information

Additional supporting information can be found online in the Supporting Information section.

21960216, 2026, 22, Downloaded from https://chemistry-europe.onlinelibrary.wiley.com/doi/10.1002/celc.70343 by Universitatsbibliothek RWTH Aachen University, Wiley Online Library on [09/11/2026]. See the Terms and Conditions (https://onlinelibrary.wiley.com/terms-and-conditions) on Wiley Online Library for rules of use; OA articles are governed by the applicable Creative Commons License